Available online at www.sciencedirect.com
SCIENCE DIRECT®
European Journal of Mechanics B/Fluids 24 (2005) 409–424

Transition to turbulence of the Batchelor flow in a rotor/stator device

A. Cros [a], E. Floriani [b], P. Le Gal [a,*], R. Lima [b]

[a] *Institut de recherche sur les phénomènes hors equilibre, 49, rue F. Joliot-Curie, BP 146, 13384 Marseille cedex 13, France*
[b] *Centre de physique théorique, CNRS Luminy, case 907, 13288, Marseille cedex 9, France*

Received 22 June 2004; received in revised form 8 October 2004; accepted 3 November 2004

Available online 22 December 2004

Abstract

This experimental study is devoted to the transition to turbulence of the flow confined between a stationary and a rotating disk. Using visualization and video image analysis, we describe the different transitions occurring in the flow as the rotating velocity of the disk is varied. The space–time behavior of the wave patterns is analyzed using the Bi-Orthogonal Decomposition (BOD) technique. This decomposition of the experimental signals on proper modes permits to project the dynamics of the waves in a reduced embedding phase space. By this means, a torus doubling bifurcation is revealed before its complete destruction during the transition to a weak turbulence. Finally, a more classical 2D-Fourier analysis completes our description of the transition and shows for higher rotation rates, the appearance of a more developed turbulence issued from the former chaotic waves.

1. Introduction

The transition to turbulence of rotating disk flows is one of the most classical but also challenging problems of fluid mechanics. Beside the fact that these flows are often met in industrial or in geophysical situations, they are also generally used to model three-dimensional boundary layer transitions (see for instance the recent review article by Reed, Saric and White [1]). When a disk rotates at a rate Ω in front of another fixed one, forming a usually called rotor/stator device, different types of flows can take place depending on the distance h between the disks and on the characteristic boundary layer thickness $\delta = \sqrt{\nu/\Omega}$ on each disk, ν being the viscosity of the fluid between the disks. When h and δ are of the same order of magnitude, the flow resembles a Couette flow and the transition to turbulence occurs via a Spatio-Temporal Intermittency scenario [2]. On the contrary, when the rotating disk layer – called the Ekman [3] or the von Karman [4] layer – is separated from the fixed disk layer – called the Bödewadt layer [5] – the flow consists of these two boundary layers separated by an inner rotating core. These typical flows are said to be of Batchelor type, as Batchelor [6] expressed for the first time the self-similar velocity fields in the case of infinite radial extension of the flows. Many authors have then analyzed the stability of these flows and two types of waves (type I and II) have been revealed in both boundary layers. For instance, Faller [7], Pikhtov and Smirnov [8], Lingwood [9] and Pier [10] performed linear stability analyses of the different velocity profiles that occur in the different regions of the flow. More recently, and following the pioneer work of Lingwood [9], Serre et al. [11] studied theoretically and numerically the transition from convective to absolute instability of these flows. Experimentally, Savaş [12,13] followed by Itoh [14,15] were the first to

* Corresponding author.
E-mail address: legal@irphe.univ-mrs.fr (P. Le Gal).

0997-7546/$ – see front matter
doi:10.1016/j.euromechflu.2004.11.002

visualize the different waves occurring in a rotor/stator system. The complete transition diagram was then built by Schouveiler, Le Gal and Chauve [16] as function of the ratio h/δ of the cavity and of the Reynolds number $Re = \Omega R^2/\nu$ (R being the radius of the disk). These authors show that the transition to turbulence of the Batchelor flow is preceded by the appearance of two types of waves: circular waves that propagate from the edge of the disk to the center (see also [17]) and spiral waves that appear at the periphery of the flow [18]. These waves were also reproduced in the numerical simulations of [19,20] .

This study is the continuation of the work of Schouveiler et al. [16] and focuses on the description of the successive bifurcations and the appearance of disordered regimes created by the interaction of the circular and the spiral waves. For this purpose, the experimental device is the same (with only slight modifications reported in Section 2) as the one used in [16]. With the help of video analysis we build space–time diagrams that record the wave dynamics on circles situated in the waves interaction region. These diagrams are first analyzed by a projection of the data onto their proper modes. This method called the Bi-Orthogonal Decomposition [21] is an extension of the Proper Orthogonal Decomposition (POD) of Lumley [22] and is sometimes also referred as the Karhunen–Loève decomposition from [23] and [24]. We show that the dynamics of the circular and spiral waves is confined on a torus that exhibits a period doubling before the appearance to weak turbulence. Finally a transition towards a more developed turbulence is described via the calculation of the bi-dimensional spectra of the space–time diagrams.

The article is organized as follows: the main characteristics of our experimental device are described in Section 2, then Section 3 reports the phenomenology of the transition whereas Sections 4 an 5 are devoted to the BOD and to the Fourier analyses respectively.

2. Experimental device

The experimental device (Fig. 1) consists of a water-filled cylindrical casing in which the rotating disk is immersed. The top lid of the container plays the role of the stationary disk. The radius R of the stainless steel disk is 140 mm and its thickness is 13 mm. It is painted in black to enhance visualization. The drive shaft goes through the bottom of the tank and is connected to a d.c. electric motor whose rotating velocity can be varied from $\Omega = 0$ to 200 rpm. The rotation frequency is measured with an optical encoder with an accuracy better than 0.2%. The stationary disk is a 20 mm thick plexiglass plate, so that the flow can be observed through it. In the present study, the distance between the rotating disk and the fixed one is set to 16 mm. Geometric imperfections, including the flatness and roughness defects were measured to induce a variation of the inter-disk distance h of less than 0.07 mm. Moreover, in order to get well-defined boundary conditions on the edge of the disk, a cylindrical sidewall is fixed to this top cover: this permits to reduce the radial space between the rotating disk and the sidewall to 0.5 mm. Note that in Schouveiler's experiment this gap was equal to 0.1 mm; however, except from small threshold variations, this change in radial gap conserves the general picture of the transition. This housing is completely filled with water at room temperature and the experiments were performed at a constant temperature of 20 °C to within ±1 °C, so that the kinematic viscosity of the

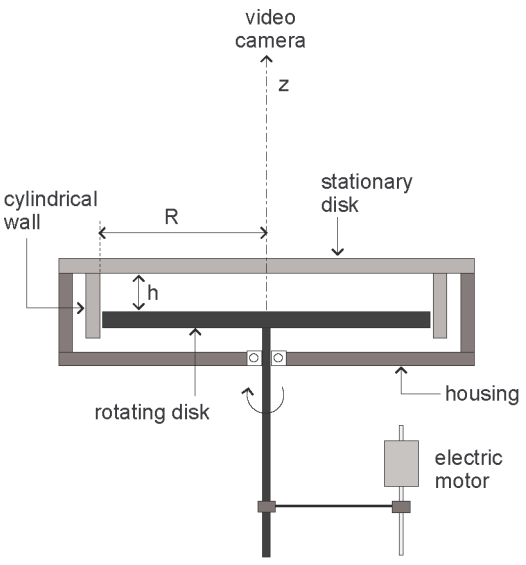

Fig. 1. Experimental device.

working fluid is 1 $mm^2\,s^{-1}$. Visualizations are realized with kalliroscope flakes. These particles are constituted by small plates of mica coated with titanium dioxide and tin oxide to assure a high reflective index. Due to their anisotropy, these flakes tend to align themselves along stream surfaces (the normal direction of flakes pointing in the direction of the velocity gradient), thus becoming visible under appropriate lighting conditions. The flow is illuminated with a circular neon tube that is positioned just above the plexiglass lid. Note that this tube was specially designed to minimize any nonaxi-symmetry defect, in particular at the electrodes junction. A CCD video camera is placed on the rotation axis and can rotate if necessary with a velocity that can be adjusted in order to observe the waves in their rotating frame. This video camera is finally connected to a computer, and images can be captured in real time.

3. Visualizations of the flow patterns and phenomenology of the transition

When the angular velocity of the disk becomes larger than 4 rpm, coherent structures appear in the Bödewadt boundary layer (see Fig. 2). Roughly, as Reynolds number grows, one can see circular and then spiral structures appear. Note that the circular waves exhibit an azimuthal modulation which breaks the rotational symmetry of the observed pattern. This loss of axi-symmetry of the pattern comes in fact from pairings observed first by Cousin-Rittemard [26] and Schouveiler et al. [16]. Note also that these images show the wave pattern in the region that is close to the fixed transparent disk. They do not give depth averaged information and a full connection between this flow visualization technique and the real flow is not yet available [25]. However, a full anemometry characterization of the different waves was already performed in [27]. The interpretation of the images is thus not straightforward although the amplitude and phase of the waves are recovered. Fig. 3 shows in particular that the Hopf bifurcation of the spiral waves is correctly determined since the square of the grey modulation amplitude, obtained by Fourier Transform (see later) is proportional to the distance to the threshold. This situation corresponds to Ω going from 5 to 14 rpm. For larger Ω, the flow appears more and more disordered, and for Ω larger than 20 rpm coherent structures are hardly recognizable in a state of weak turbulence. In the following we will keep, for convenience, Ω as the control parameter of our system. Time will be expressed in number of disk rotations and the frequency unit of the hydrodynamical modes will be the inverse disk rotation duration.

As the flow is nonhomogeneous in the radial direction, the circular waves appear at the periphery of the disk and propagate towards the center. It has been shown in [17] that these circular waves are of convective type. So, apart from the very central region of the flow, they can be detected everywhere in the flow with a variable amplitude. Spiral waves appear through a Hopf bifurcation in the form of a global mode with a spatial three-dimensional envelope [27]. Thus, there is a unique threshold (independent of the measurement position) for the bifurcation of this spiral mode which is characterized by an azimuthal wave number and a frequency. When both modes are present, they coexist in the flow for Ω going from 10 to 14 rpm with amplitudes varying along the radius. However, as it can be seen on Fig. 2, in a region extending approximately between $0.6R$ and $0.8R$,

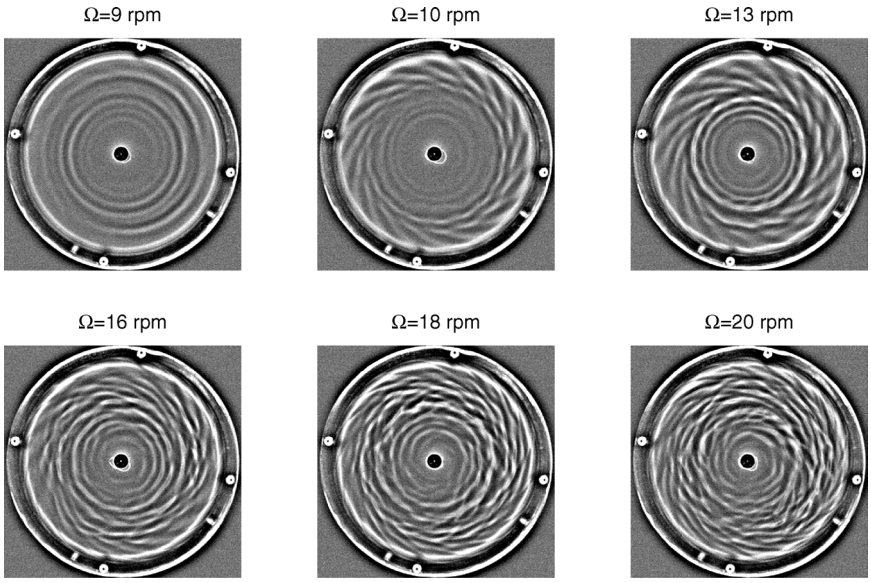

Fig. 2. Images of the flow for some values of Ω, the angular velocity of the disk. Clockwise rotation.

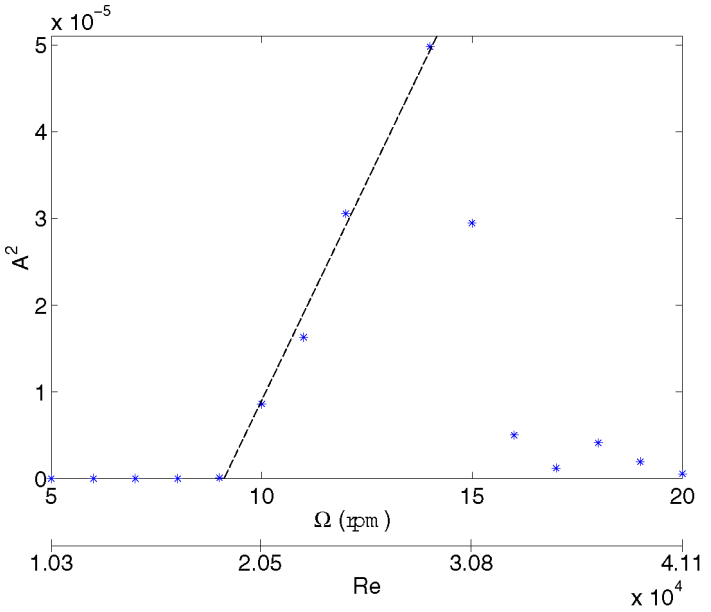

Fig. 3. Squared amplitude of the grey level fluctuations corresponding to the spiral waves versus Ω; the typical linear behavior corresponding to the Hopf bifurcation is recovered.

the flow patterns are not affected by boundary conditions and seem quite homogeneous, at least visually. Although we cannot prove that the subsequent bifurcated modes will be of global type (with a unique threshold independent of the radial position), we expect anyway their characteristics to be typical of the transition. Threshold variations, if any, along the radial position, will be in a range of 10% around that detected in the middle of the considered region. Therefore, in order to decrease the huge quantity of data recorded in films, we choose to observe the system at a fixed radius $r = 0.7R$. Thus we only analyze data along the homogeneous direction (θ) as function of time and for each fixed value of Ω. However, although we did not describe in detail the sequence of bifurcations at different radial positions, we have checked qualitatively that the global flow transition is independent of the data acquisition circle (at least for radii between $0.6R$ and $0.8R$). The gathering of the data recorded on the circle $r = 0.7R$ gives spatio-temporal diagrams that will be used to study quantitatively the transition. These spatio-temporal diagrams have a duration of 40 s for 2048 temporal data points. Their spatial resolution is 1.2 mm on 512 spatial points. Figs. 4 and 5 are only temporal windows of constant duration equal to 4 disk rotations. Therefore, varying the angular velocity Ω of the rotating disk, we progressively pass from a laminar to a chaotic flow. For this particular value of the radius, circular waves are present for 5 rpm $\leqslant \Omega \leqslant$ 9 rpm, spiral waves appear at $\Omega = 10$ rpm and keep their coherence up to approximatively $\Omega = 15$ rpm (see Fig. 4). Then dislocations appear in the flow and a fully chaotic behavior is reached for $\Omega = 18$ rpm, as it can be seen in the space–time diagrams showing the dynamics of the waves (see Fig. 5). Corresponding to each of these diagrams, a temporal Fourier spectrum, averaged on the spatial direction θ, permits to evaluate the growing complexity of the dynamics. As shown on the first diagram ($\Omega = 9$ rpm) of Fig. 4 and except for a slight spatial undulation due to waves pairing (see [16]), the circular waves appear as vertical stripes in the spatio-temporal diagrams. Their propagation towards the center of the disk is associated to three frequencies ν at 1, 2 and 3 times the disk rotation frequency. Then for $\Omega = 10$ rpm, the spiral waves, seen as 17 tilted thin stripes, appear. Their frequency ν is equal to 2.1 and higher harmonics appear as Ω is increased. For $\Omega = 16$ rpm, last diagram of Fig. 4, it can be seen that the wave pattern is no more periodic in time or in space and the dynamics of the still visible structures is no more regular.

At higher rotation rates, the coherence of the pattern will be completely lost, as it can be observed on Fig. 5. More and more peaks appear in the Fourier spectra, as it is particularly visible for $\Omega = 20$ rpm, where the flow has definitively lost its organization.

Our aim is now to discuss this transition in a more quantitative way. As far as experimental data are concerned, our space–time diagrams give information on 512 values of the spatial coordinate θ, for 2048 instants in time: data form a 512×2048 matrix $u(\theta, t)$. To have more insight in the space–time dynamics of the system, we use a bi-orthogonal decomposition (BOD) of the former space–time diagrams in order to observe the dynamical system history in its phase space.

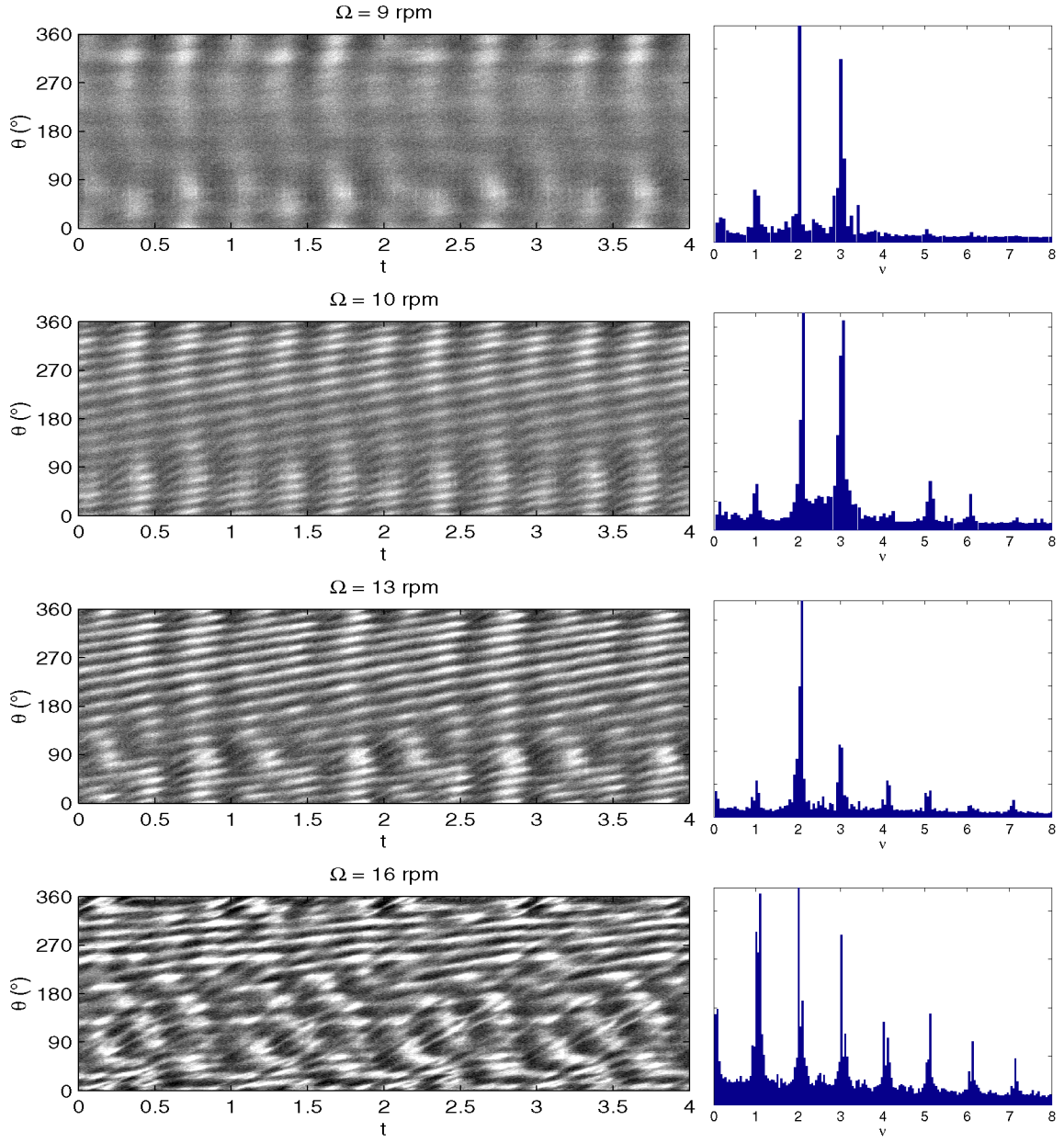

Fig. 4. Windows of space–time diagrams on the circle $r = 0.7R$, for some typical values of the angular velocity Ω and for a duration of 4 disk rotations. We also show in arbitrary linear scale, the corresponding temporal Fourier spectra averaged on θ.

4. Phase-space analysis of the transition

In what follows we use a tool, the bi-orthogonal decomposition (BOD), that allows to describe in a simple way the dynamics of the system by identifying and treating as a whole each spatial structure as well as the corresponding time dynamics. The main idea is to look at space and time in a completely symmetrical way. It is well known that when a space–time signal acquires some modulation, either in space or time or both, the projection on Fourier modes immediately splits in a large number of components that can be difficult to analyze, especially close to resonance. Instead, by slightly adapting the space and time basis to the change of the system with the parameters, it is possible to keep the maximal simplicity of description (for instance the dimension of the space and time representation) as long as the topological properties of the dynamics do not change. This is a big advantage if we are precisely interested in detecting and describing the bifurcations undertaken by the system when a parameter (as the

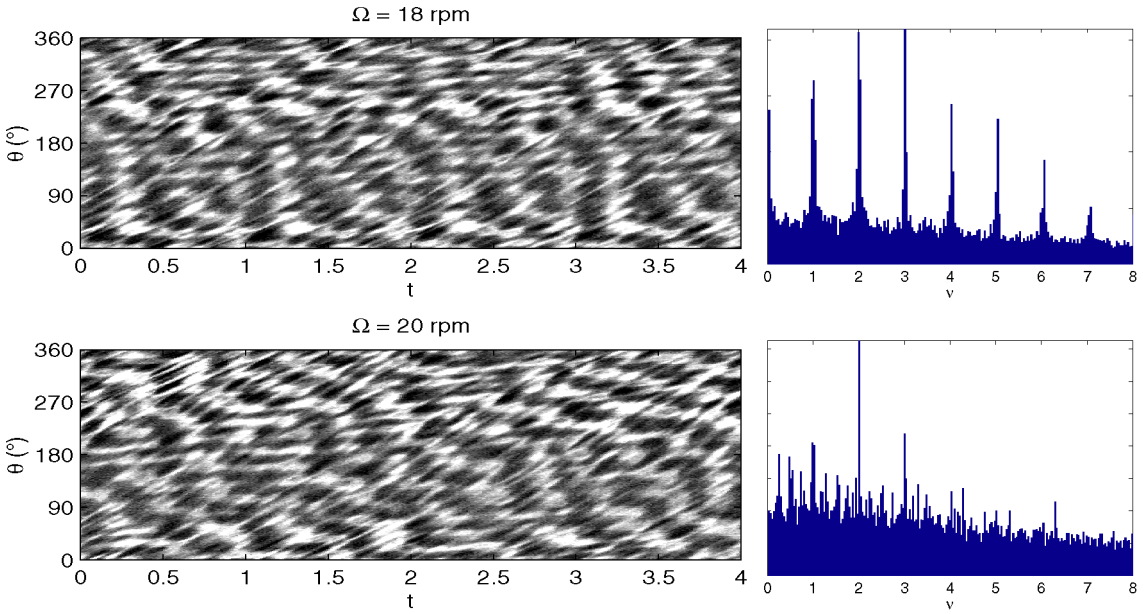

Fig. 5. Space–time diagrams on the circle $r = 0.7R$, for higher values of the angular velocity Ω (18 and 20 rpm), for which coherent structures are not anymore recognizable (time is expressed in number of rotations and θ is the azimuthal angle). We also show the corresponding temporal Fourier spectra averaged on θ.

angular velocity of the disk in our case) changes. Of course, this analysis may be completed, as we shall do in what follows, by any other complementary tool, in particular a space–time Fourier analysis. By combining the BOD, that allows to distinguish the different dynamical structures in the fluid, with a Fourier analysis, we were able to identify the scenario of the transition towards a chaotic flow in the rotor/stator device studied in this work.

For the sake of completeness we recall that (see [21]), for an extended system described by signals $u(x,t)$, the BOD establishes a correspondence between the phase space $\chi(X)$ where the orbit ξ_t evolves (where for each t, ξ_t is the function $\xi_t(x) = u(x,t)$) and the space $\chi(T)$ of the corresponding time series η_x (where for each x, η_x is the function $\eta_x(t) = u(x,t)$). In fact, $\chi(X)$ is the smallest linear space containing the ξ_t and, symmetrically, $\chi(T)$ is the smallest linear space containing the η_x. This is why $\chi(X)$ and $\chi(T)$ are good candidates for the description of space–time dynamics. Further, a convenient way of describing these two spaces is given by two particular orthogonal bases of vectors: the topos ϕ_k generating $\chi(X)$ that are, in our case, the right eigenvectors of the matrix u, and the chronos ψ_k generating $\chi(T)$ that are the left eigenvectors. As a consequence, the dimensions of $\chi(X)$ and $\chi(T)$ are equal, being both equal to the rank of u; it is even possible to show that the BOD gives a one-to-one correspondence between the ϕ_k's and the ψ_k's. Moreover, these proper modes can be ordered by their decreasing energy (or eigenvalue) and therefore labelled by an index k.

Notice that the curve ξ_t is just the trajectory of the system, in the usual sense, in the phase space $\chi(X)$. Conversely, and this representation is far less common, the curve η_x represents a time series array in the corresponding space $\chi(T)$. In this context $u(x,t)$ is also a kernel of an isomorphic map from $\chi(X)$ to $\chi(T)$ and therefore the corresponding spectral analysis reads

$$u(x,t) = \sum_k \lambda_k \varphi_k(x) \psi_k(t),$$

where the positive numbers λ_k are the eigenvalues and $\varphi_k(x)$ (resp. $\psi_k(t)$) form an orthogonal basis of the phase space $\chi(X)$ (resp. time series space $\chi(T)$). Notice that any truncation of the previous sum is an approximation of the signal – in fact the best among all the approximations with the same number of orthogonal terms – but it is at the same time an orthogonal projection of the orbit on a lower dimensional sub-space (both of phase space and of time series space).

We will describe in the following paragraphs how instabilities and coherent structures manifest themselves in the projection of these two spaces on small subspaces, by taking 3-dimension projections of $\chi(X)$ and $\chi(T)$. We disregard the first eigenvector ϕ_1, ψ_1, relative to the maximal eigenvalue, because it is associated to the mean gray level in the image acquisition. The reason to take the next 3-dimensional space as a basis for our analysis is twofold. First because the four largest eigenvalues represent about 60 percent of the total spectrum, which implies that the distance of the real orbit to its projection on such a subspace is not very large. Second, and more important, due to the wavelike form of the signal, the essential features of the dynamics are captured in the subspace we analyze: indeed, for a pure travelling wave, it is known that the BOD forces the dynamics on the

subspaces corresponding to smaller eigenvalues to be a mirror of the dynamics on the subspace of the larger eigenvalues [28]. In our case, the modulation of travelling waves merely deforms this mirror image.

4.1. Circular waves

The BOD analysis shows that the trajectory in phase space relative to all the values of Ω such that only circular waves are present is periodic, being represented by a closed curve. However, the number of frequencies characterizing the motion varies with Ω.

For $\Omega = 6$ rpm let us consider the projection $\xi_t^{2,3}$ of the trajectory on the (ϕ_2, ϕ_3) plane (see Fig. 6). It looks roughly like a circle, but so close to the bifurcation threshold, the high level of noise makes it necessary to compute the angle $\alpha(t)$ between the vectors ϕ_2 and $\xi_t^{2,3}$, in order to show that the trajectory is indeed periodic. The condition under which the trajectory is closed is that $\alpha(t)$ grows a multiple of 2π in an integer number of rounds of the disk: Fig. 6 shows that this is the case for $\Omega = 6$ rpm (and is also verified for Ω up to 9 rpm), and the value 2.03 for the slope of $\alpha(t)$ confirms the observation of 2 circular structures per round crossing the acquisition circle (see the Fourier transforms of Fig. 4).

Fig. 6 shows also that the evolution of the angle $\alpha(t)$ for $\Omega = 9$ rpm is not monotone anymore; correspondingly, the trajectory $\xi_t^{2,3}$ shows two or three loops. Nevertheless, this is not the expression of a topological change, but only translates the fact that for this value of the angular velocity of the disk, and for $r = 0.7R$, one observes in the Bödewadt layer three circular waves merging to give two circles per rotation: as it appears from the Fourier transforms of Fig. 4, the three commensurable frequencies $\nu = 1, 2, 3$ characterize the system (see also [16]). Indeed, if we consider one more dimension by projecting the trajectory on (ϕ_2, ϕ_3, ϕ_4), as it is done in Fig. 7, it appears that $\xi_t^{2,3,4}$ describes a closed curve (a limit cycle) evolving on a torus. Note that the shape of the orbit in the (ψ_2, ψ_3) plane (Fig. 6) is due to the loss of axi-symmetry of the circular wave pattern as already mentioned. For instance, for $\Omega = 6$ and 9 rpm, a limit cycle takes place instead of a single dot as it should be obtained if the circular waves were perfect circles. For Ω equal or larger than 10 rpm, a rotation with a frequency equal to 17, that is the total number of spiral arms, can be measured on the variation of a rotation angle $\beta(\theta)$: a second Hopf bifurcation occurred in the flow and the following section presents the study of the subsequent pattern.

4.2. Spiral waves

Figs. 6 and 7 clearly indicate that a qualitative change in the structure of trajectories takes place for $\Omega = 10$ rpm. In particular, the vector $\xi_t^{2,3,4}$ in Fig. 7 does not anymore describe a closed trajectory in the space (ϕ_2, ϕ_3, ϕ_4). In fact, spiral waves appear with a frequency $\nu_s = 2.1$ that is incommensurable to the frequencies 1, 2, 3 of circular waves (see Fig. 4). The trajectory still evolves on a torus, but it is not periodic anymore. The fact that the two systems of waves are unlocked translates a particular characteristic of the hydrodynamic system under study. Indeed, if circular and spiral waves where locked in phase, a particular phase lag would be chosen: this is clearly forbidden, since the phase of the spirals winds up along both the time and the θ axes and the phase of the circular waves which does not propagate along the θ axis.

Let us stress that bare one-dimensional Fourier analysis does not give any clear indication of the appearance of spiral waves, due to the fact that their temporal frequency happens to be very close to that of circular waves, so that Fourier spectra in Fig. 4 for $\Omega = 9$ rpm and $\Omega = 10$ rpm look very similar. Here a reliable indicator of such a transition is the dramatic change in $\chi(X)$ at this value of Ω, as it can be seen directly from the shape of ϕ_2, ϕ_3, ϕ_4 for $\Omega = 9$ rpm and $\Omega = 10$ rpm (see Fig. 8). We will see later that a 2D-Fourier analysis can separate the different modes, but in this case we have to deal with the problem of filtering the pertinent modes in order to build a reduced phase-space.

Spiral and circular waves coexist for $\Omega = 10$ rpm up to $\Omega = 15$ rpm. Starting from $\Omega = 11$ rpm, the torus in space (ϕ_2, ϕ_3, ϕ_4) changes of orientation: its axis becomes orthogonal to the plane (ϕ_2, ϕ_3), so that the projection $\xi_t^{2,3}$ looks again like a circle; the slope of the angle $\alpha(t)$ is close to 2.1 that is the value of the spiral frequency (see Fig. 6).

The other frequency generating the (ϕ_2, ϕ_3, ϕ_4) torus, which must correspond to one of the frequencies of circular waves, can be observed trough the motion in a Poincaré section of phase space. We have calculated the first intersections of the trajectory with the plane $\phi_2 = 0$: the distance δ between consecutive intersections gives a measure of the fractional part of ν_1/ν_2, the ratio of the two incommensurable frequencies generating the torus. δ fluctuates between 0.04 and 0.13, which is compatible with $\nu_1 = \nu_s = 2.1$ and $\nu_2 = 2$.

4.3. Bifurcation of invariant torus

We shall see that the second major change in the dynamics, after the appearance of spirals for $\Omega = 10$ rpm, takes place around $\Omega = 15$ rpm. In fact, for $\Omega = 16$ rpm, the absolute value of the average slope of $\alpha(t)$ takes the value 1.08 (see Fig. 6), about half of the value it had for lower Ω. This means that the time it takes for the quasi-periodic trajectory to turn around the torus in space (ϕ_2, ϕ_3, ϕ_4) doubles.

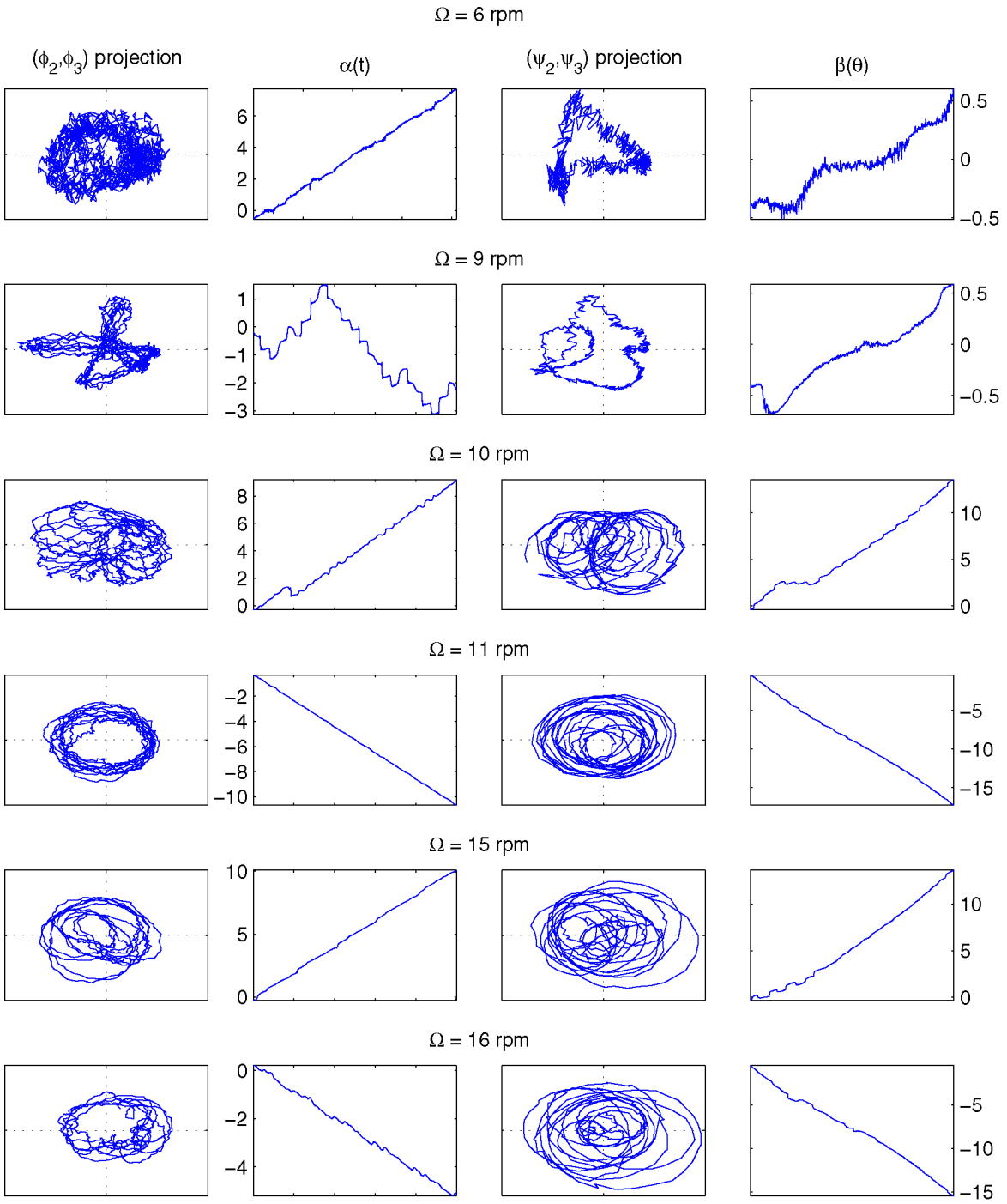

Fig. 6. Left column: projection of $u(\theta, t)$ on (ϕ_2, ϕ_3) for typical values of Ω (the horizontal and vertical axis correspond to a fixed interval $[-0.07, 0.07]$). Second column: angle $\alpha(t)$ (in units of 2π) between the horizontal axis ϕ_2 and $\xi_t^{2,3}$, as a function of time during 5 disk rotations. Third column: projection of $u(\theta, t)$ on (ψ_2, ψ_3) (the horizontal and vertical axis correspond to a fixed interval $[-0.13, 0.13]$). Fourth column: angle $\beta(\theta)$ (in units of 2π) between the horizontal axis ψ_2 and $\eta_\theta^{2,3}$, as a function of θ.

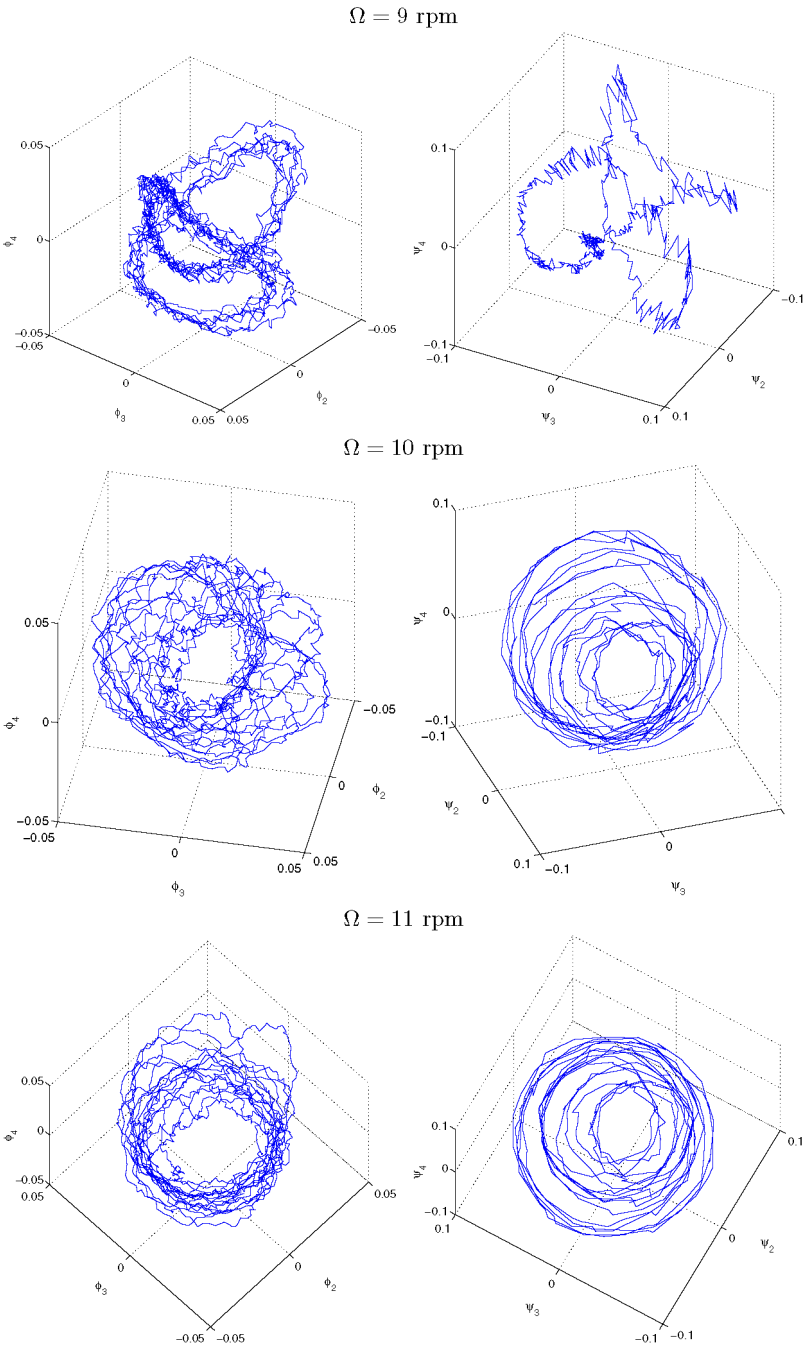

Fig. 7. Left column: projection of $u(\theta, t)$ on (ϕ_2, ϕ_3, ϕ_4) for $\Omega = 9, 10, 11$ rpm. Right column: projection of $u(\theta, t)$ on (ψ_2, ψ_3, ψ_4) for $\Omega = 9, 10, 11$ rpm.

This is the consequence of a bifurcation of invariant tori [29], that has been recently observed in several experimental situations: in an electrochemical reaction [30], in liquid gallium convection [31], in a double pendulum oscillations [32], in Rayleigh–Bénard convection [33], in a ferroelectric phase transition [34] or in a Taylor–Couette flow [35].

This bifurcation has been theoretically studied in the context of normal forms of maps. Let us recall what happens in the case of the usual period doubling bifurcation. Before the bifurcation, the system is on a stable limit cycle in phase space, of period T; this corresponds to a stable fixed point in a Poincaré section. When the control parameter reaches the bifurcation value, this

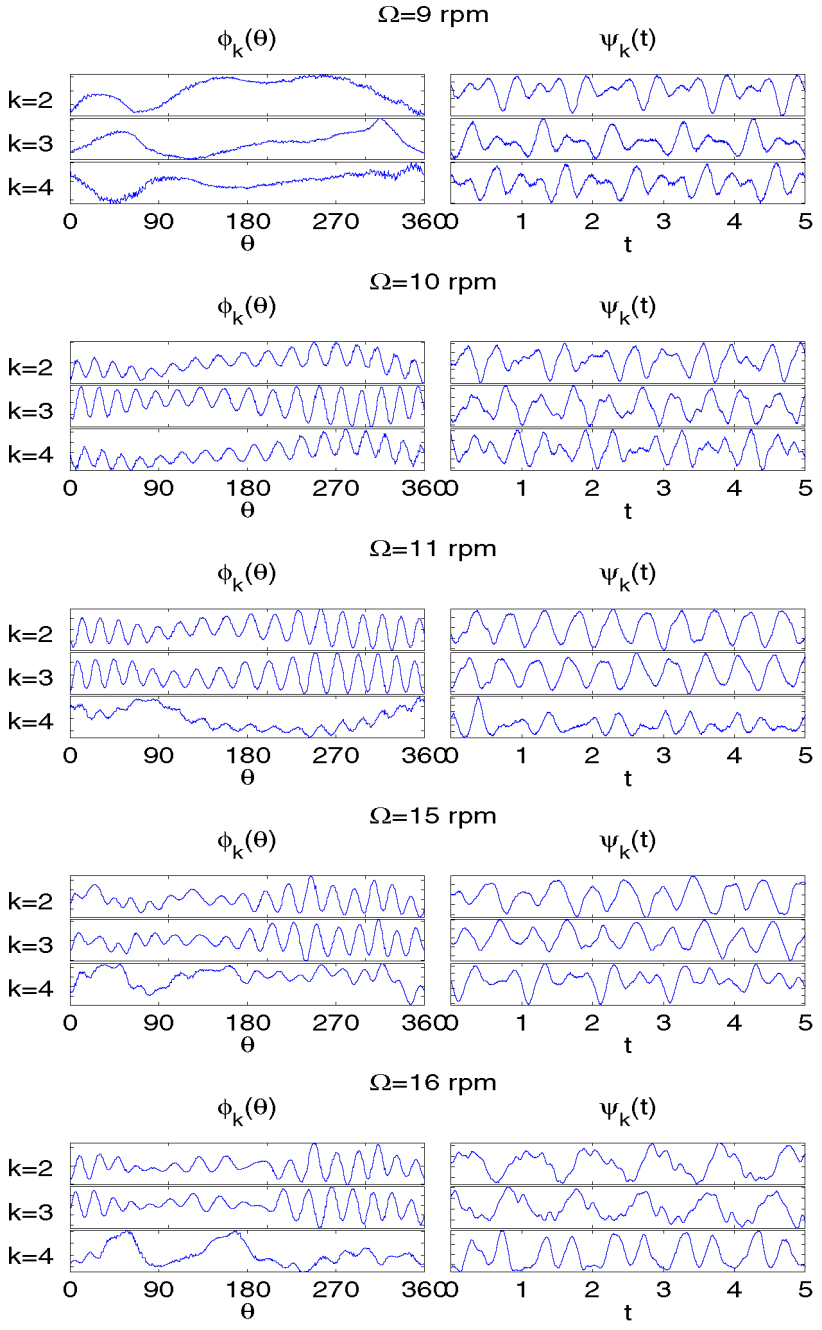

Fig. 8. Plot of the first three topos and chronos for $\Omega = 9, 10, 11, 15, 16$ rpm.

fixed point becomes unstable, and a stable 2-cycle appears in the Poincaré section, corresponding to a new limit cycle of period $2T$ in phase space. (The application describing the dynamics in the Poincaré section is essentially a logistic map.)

In a similar way, in our case, before the bifurcation the quasi-periodic trajectory of the system lives on an invariant torus in phase space, which corresponds to a limit cycle in a Poincaré section. When the control parameter reaches the bifurcation value, this limit cycle persists but becomes unstable, and a couple of stable cycles appears, the trajectory passing once in cycle 1 and once in cycle 2 each time it crosses the Poincaré section. This corresponds to a folding of the torus in phase space.

Notice that the essential theoretical ingredient for the existence of such a bifurcation [29], is the existence of the limit cycle in the Poincaré section above its instability threshold. In the framework of the theoretical study presented by Iooss and Los in

1988 [36], this is a rather delicate point to prove, since it depends on the arithmetic properties of the rotation number. In our case, the existence of the unstable limit cycle above the bifurcation could instead be related to the rotation symmetry in phase space (reflecting the corresponding symmetry of the hydrodynamical system).

Let us point out that, the system having more than one characteristic frequency before the bifurcation, there is no fixed rule establishing which one of them (or which linear combination of them) will be divided by 2 as the system undergoes the bifurcation. In our case, it is the frequency of spiral waves that passes from 2.1 to 1.08, so that the torus in space (ϕ_2, ϕ_3, ϕ_4) must fold in a parallel direction to the (ϕ_2, ϕ_3) plane.

Once again, let us remark that it would be difficult to detect the bifurcation by Fourier analysis alone, due to the fact that 1.08 is very close to the frequency 1 of circular waves, so that Fourier spectra for $\Omega = 14$ rpm to $\Omega = 16$ rpm look very similar.

The total number of spiral structures (17 on the acquisition circle) does not vary as the bifurcation takes place. As a consequence, the doubling of the temporal period of spirals must be related either to a decrease of their phase velocity or to an increase of the angle they form with the acquisition circle. The visualizations of the flow seem to confirm the second hypothesis, even if it is not possible to define precisely a critical radius at which spiral structures suddenly change of orientation. Instead, by observing such a change for a given fixed radius, as we do in this work, we may be able to detect this bifurcation with a good accuracy.

Let us now then look more carefully at the way this bifurcation manifests itself in our phase space. Our initial observation of a change in the dynamics, namely, the fact that for $\Omega = 16$ rpm the slope of $\alpha(t)$, the rotation angle in the (ϕ_2, ϕ_3) plane, is half of what it was for $\Omega = 15$ rpm, means that the torus in space (ϕ_2, ϕ_3, ϕ_4) has in fact already completely unfolded at $\Omega = 16$ rpm. The exact value of Ω for which it doubles its period, is then certainly smaller that 16 rpm. So, let us look closely at what happens for $\Omega = 15$ rpm: we label the points separated by the same time delay, here equal to the period T of the dynamics on the torus before the bifurcation, $T = 1/2.1$ units. The separation of odd and even points shows on Fig. 9 the folding of the torus in a new stable torus corresponding to a doubling of the period, and the consequent destabilization of the former. This bifurcation is confirmed by the position of the same points for $\Omega = 16$ rpm (see Fig. 10), now alternating in opposite small regions of the phase space corresponding to this value of the control parameter, showing the complete unfolding of the torus, and causing the change in the behavior of $\alpha(t)$.

A particular feature of the system we study is that, for the value $\Omega = 16$ rpm just following the bifurcation, small loops appear in the trajectory (Figs. 6 and 10), during which the sign of the angle $\alpha(t)$ changes. They correspond to phase defects. In fact, for values of Ω larger than 16 rpm, loops become larger and the trajectory spends larger times on them. The flow becomes more and more disordered, without undergoing any other distinguishable period doubling.

Notice that, according to the theory, the number of successive period doubling bifurcations before transition to chaos is not predicted in general. In fact, the transition itself is due to the breaking of invariant tori, as in the Ruelle–Takens–Newhouse [37] scenario, and not, in general, to an infinite sequence of period doubling bifurcations [38]. In this case, chaos would therefore be

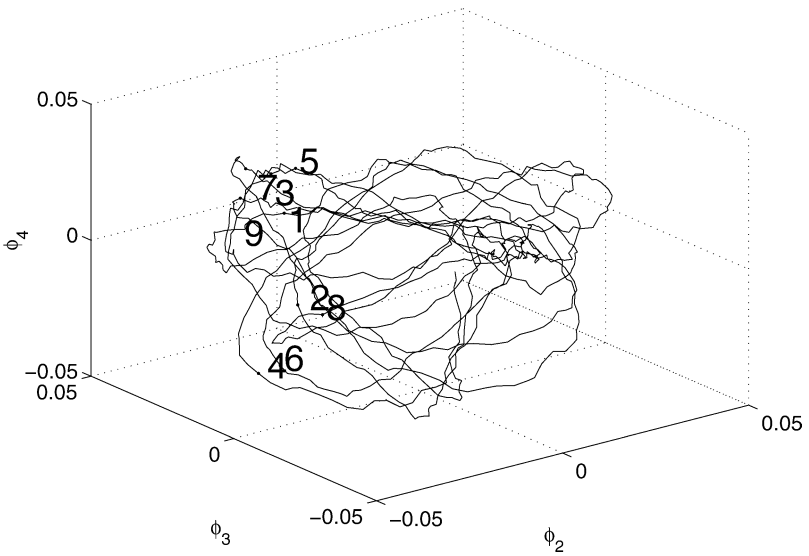

Fig. 9. Projection of $u(\theta, t)$ on (ϕ_2, ϕ_3, ϕ_4) for $\Omega = 15$ rpm. In the picture, we labelled the points of the orbit separated by a same time delay equal to the period T of the dynamics on the torus before the bifurcation. The separation between odd and even loops is clearly visible: the torus doubling bifurcation just happened.

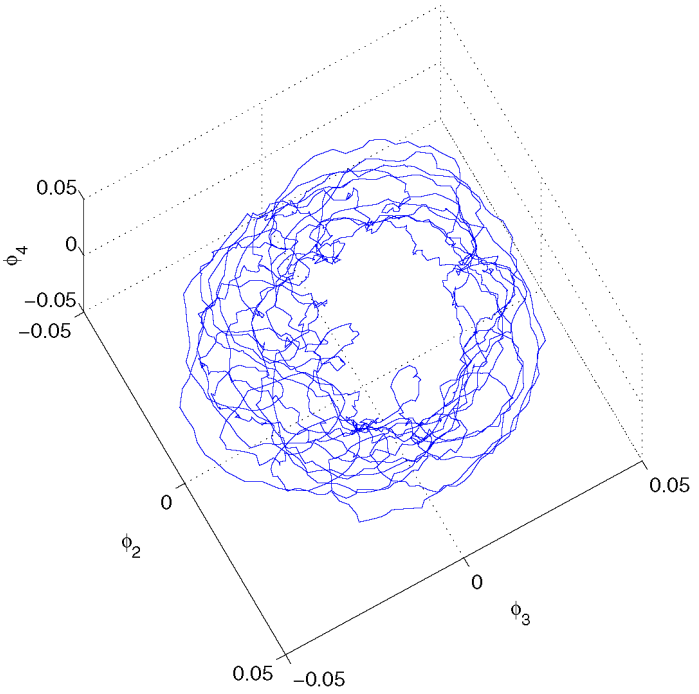

Fig. 10. Projection of $u(\theta, t)$ on (ϕ_2, ϕ_3, ϕ_4) for $\Omega = 16$ rpm. The trajectory mainly winds up around the torus but small loops escaping from this torus are visible.

a consequence of the loss of smoothness of invariant surfaces at each period doubling, leading to the breaking of the torus, so that the observed number of such bifurcations is not universal. Discussing this issue in our system would definitely deserve a more detailed experimental investigation close to the critical value of Ω.

Note that the transition to chaos via the destruction of tori without torus doubling was recently discovered in a flow which is similar to the one investigated [39]. In their case, the rotating flow was created between two rotating spheres and spiral patterns similar to what we observe between rotating disks, transit to chaos.

For higher values of Ω, the flow and thus the trajectories in the phase space are more and more disordered. The following section describes the final transition from the chaotic flows that were previously described and a more developed turbulence which takes place in the gap between the disks. With this aim, a Fourier analysis of the space–time diagrams of Figs. 4 and 5 (and completed by higher values of Ω) is performed.

5. Fourier analysis of the transition to turbulence

In fact, the calculation of the 2D-Fourier spectra of the spatio-temporal diagrams leads to the dispersion relation of the waves in the plane (ν, k) where ν is the frequency of the waves and k their azimuthal wave numbers. Fig. 11 presents the evolution of these dispersion relations as Ω is increased. Because of the central symmetry of the Fourier transform, each peak in the spectra possesses a symmetric one with respect to the origin. Thus each mode is associated with a couple of peaks.

At $\Omega = 9$ rpm, beside the zero frequency associated with the continuous grey level background of the images, two wave packets localized around $k = 0$ and $\nu = -2$ or 2, are clearly visible: they represent the propagation of the circular waves in the flow. At $\Omega = 10$ rpm, two new peaks representing the spirals appear in the spectra. They are centered around $k = \pm 17$ and $\nu = \pm 2.1$. Note that each peak appears to be separated in two parts. This comes in fact from the slight modulation of the circular waves along the acquisition circle. For $\Omega = 10$ rpm and 13 rpm, one can also see other wave packets located in $k = 17$ and $\nu = -5.1$, $\nu = -8.2$ (and their symmetric peaks). These wave packets translate the nonlinear interaction between the spiral waves and the circular waves. For Ω greater than 15 rpm, these nonlinear interactions give birth to three inclined stripes in the spectral plane. Two of these bands are symmetric with respect to the center, and pass through the former peaks representing the spiral and the circular waves. Moreover, a third packet, having also an elongated shape aligns parallel between the former ones. This band clearly indicates the formation of a low frequency mode coming from the quadratic nonlinear interaction of the waves: any combination of two modes belonging to each of the side bands, generates a mode belonging to the central

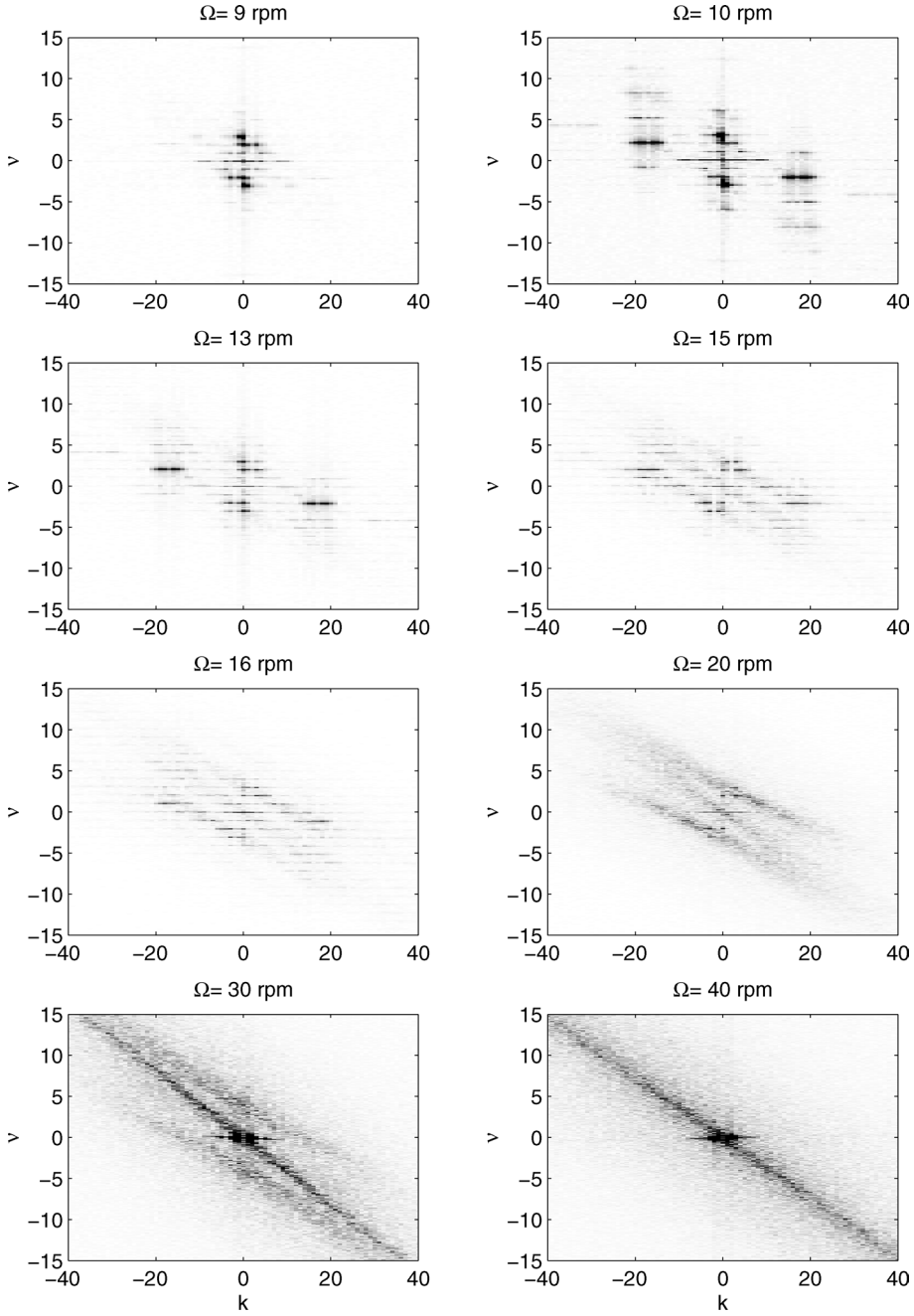

Fig. 11. 2D-Fourier spectra of space–time diagrams for $\Omega = 9$ to 40 rpm.

low frequency band. As it can be seen on Fig. 11, the intensity of the central wave packet grows with the rotation rate and at $\Omega = 17$ rpm, its intensity is comparable to the one of the side bands. Note also that its angle with respect to the axes has changed: it is no more parallel to the wave packets that were at its origin. The two last images of Fig. 11 show the 2D-Fourier spectra for higher rotation rates. As presented, the side packets, representing the circular and the spiral waves disappear. For $\Omega = 30$ rpm only a single packet passing through the origin is present. As this wave packet is a straight line, its slope is the group velocity of the waves (projected on the azimuthal direction) that constitute the weak turbulence regime. Thus this packet, born from the nonlinear interactions of the unstable modes (the circular and the spiral waves) travels at a group velocity whose value progressively changes from the azimuthal group velocity given by the wave dispersion relation to a value which,

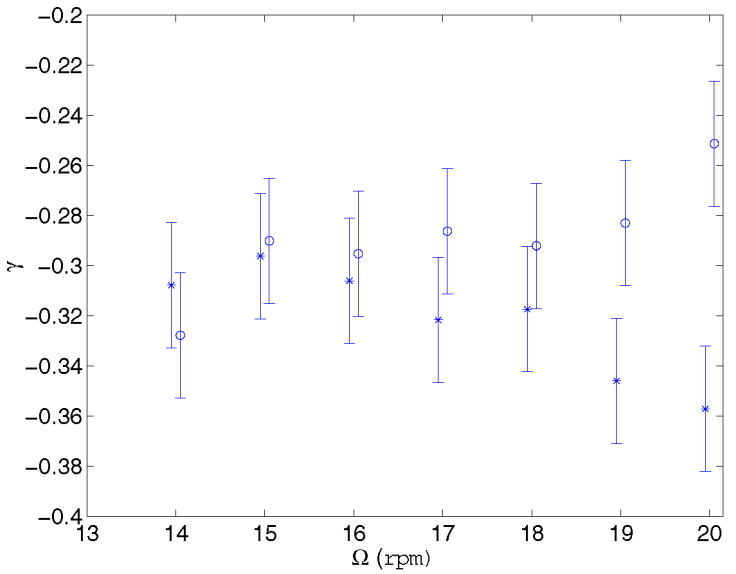

Fig. 12. Azimuthal group velocity of the wave packets versus rotation rate Ω. (∗) central wave packet, (∘) side wave packets. The central packet is entrained with the mean azimuthal velocity of the turbulent flow (between 0.3 and 0.4Ω).

according to the Taylor hypothesis of frozen turbulence, is equal to the mean velocity of the flow. Indeed, Fig. 12 shows the slopes γ made by the central and by the side packets as a function of the rotation rate. These slopes represent azimuthal group velocities and can be normalized by the local disk velocity (ΩR, with $R = 0.7$). The error bars give the standard deviation of the data obtained from different measurements. As it can be seen on Fig. 12, the azimuthal group velocity of the central and of the side packets are similar up to $\Omega = 15$ rpm. Then both curves separate, the central packet azimuthal group velocity being around -0.34, that is close to the azimuthal velocity of the fluid outside the boundary layers: Rasmussen [40] calculated for instance a value equal to 0.313 in the case of infinite disks, and Schouveiler et al. [16] measured a velocity between 0.3 and 0.4. Therefore, these measurements illustrate the smooth transition from a chaotic wavy flow (with waves possessing their own phase and group velocities) towards a more developed turbulent flow with waves travelling on average at the mean velocity of the fluid.

6. Conclusion

The projection of the signal on an optimal basis given by bi-orthogonal decomposition allows to sketch a coherent scenario of transition to turbulence for the Batchelor's flow.

The propagation of modulated circular waves starting from $\Omega = 5$ rpm gives in phase space a periodic trajectory describing a closed curve. When spiral waves appear at $\Omega = 10$ rpm, the topology of trajectories changes: since spiral waves are characterized by a temporal frequency ν_s that is not commensurable to those of circular waves, the limit cycle bifurcates to a torus.

At $\Omega = 16$ rpm, it suddenly appears in the system a frequency that is half the frequency ν_s that generated the torus: this indicates a bifurcation of an invariant torus, recently observed in other systems. For the same value of Ω, loops appear in the trajectory: they correspond to temporary changes of rotation direction in the (ϕ_2, ϕ_3) plane, and thus to phase defects in spatiotemporal diagrams. For larger values of Ω, the time the trajectory passes on the loops grows, which makes the signal more and more disordered. At the same time, the spatial structure of the flow becomes more disorganized, generating new eigenvectors ϕ_2, ϕ_3, ϕ_4, in whose space a torus is not anymore recognizable. A 2D-Fourier transform of the space–time signals permits finally to describe the slow transformation of the chaotic flow in weak turbulence and finally in a more developed turbulence. Due to nonlinear interactions between waves, the spectra in the (wave number, frequency) plane get more and more complex. The dispersion relation of the waves, first constituted by single isolated peaks, transforms in three bands and finally in a single one which is compatible with a Taylor frozen turbulence whose convective velocity is the mean velocity of the flow.

For the values of the angular velocity of the disk considered here, only one period doubling has been observed. Nevertheless, theoretical studies show that in this hybrid scenario, presenting both the features of quasi-periodicity and of doubling period cascade, chaos does not necessarily appear after an infinity of period doubling steps. In all the experiences where this scenario

is observed, the period doubling cascade is interrupted at an early stage by transition to chaotic behavior. The description of this scenario could be made more precise by raising the control parameter Ω by smaller steps, in order to determine, for example, the relation between the bifurcation and the appearance of phase defects. It would also be interesting to study the transition to chaos of this system in the case of spiral waves of larger frequency, well separated from the frequency characteristic of circular waves; the observations made in [18] on the same system show that this is possible.

References

[1] W.S. Saric, H.L. Reed, E.B. White, Stability and transition of three-dimensional boundary layers, Ann. Rev. Fluid Mech. 35 (2003) 413–440.
[2] A. Cros, P. Le Gal, Spatio-temporal intermittency in the torsionnal Couette flow between a stationary and a rotating disk, Phys. Fluid 14 (2002) 3755–3765.
[3] V.W. Ekman, On the influence of the Earth's rotation on ocean currents, Arkiv. Mat. Astr. Fys. 2 (11) (1905) 1–52.
[4] T. von Kármán, Über laminare und turbulente Reibung, Z. Angew. Math. Mech. 1 (1921) 233–252.
[5] U.T. Bödewadt, Die Drehströmung über festem Grunde, Z. Angew. Math. Mech. 20 (1940) 241–253.
[6] G.K. Batchelor, Note on a class of solutions of the Navier–Stokes equations representing steady rotationally-symmetric flow, Q. J. Mech. Appl. Math. 4 (1951) 29–41.
[7] A.J. Faller, Instability and transition of disturbed flow over a rotating disk, J. Fluid Mech. 230 (1991) 245–269.
[8] S.V. Pikhtov, E.M. Smirnov, Boundary layer stability on a rotating disk with corotation of the surrounding fluid, Izv. Ross. Akad. Nauk, Mekh. Zhidk. Gaza 5 (1992) 69–77 (in Russian);
S.V. Pikhtov, E.M. Smirnov, Boundary layer stability on a rotating disk with corotation of the surrounding fluid, Fluid Dyn. 27 (5) (1993) 657–663.
[9] R.J. Lingwood, Absolute instability of the Ekman layer and related rotating flow, J. Fluid Mech. 331 (1997) 405–428.
[10] B. Pier, Finite amplitude crossflow vortices, secondary instability and transition in the rotating disk boundary layer, J. Fluid Mech. 487 (2003) 315–343.
[11] E. Serre, E. Tuliszka-Sznitko, P. Bontoux, Coupled numerical and theoretical study of the flow transition between a rotating and a stationary disk, Phys. Fluids 16 (2004) 688–706.
[12] Ö. Savaş, Circular waves on a stationary disk in rotating flow, Phys. Fluids 26 (12) (1983) 3445–3448.
[13] Ö. Savaş, Stability of Bödewadt flow, J. Fluid Mech. 183 (1987) 77–94.
[14] M. Itoh, Instability and transition of the flow around a rotating disk in a casing, Toyota Rep. 36 (1988) 28–36.
[15] M. Itoh, On the instability of flow between coaxial rotating disks, in: ASME Boundary Layer Stability and Transition to Turbulence, FED 114, 1991, pp. 83–89.
[16] L. Schouveiler, P. Le Gal, M.P. Chauve, Instabilities of the flow between a rotating and a stationary disk, J. Fluid Mech. 443 (2001) 329–350.
[17] G. Gauthier, P. Gondret, M. Rabaud, Axisymmetric propagating vortices in the flow between a stationary and a rotating disk enclosed by a cylinder, J. Fluid Mech. 386 (1999) 105–126.
[18] L. Schouveiler, P. Le Gal, M.P. Chauve, Stability of a traveling roll system in a rotating disk flow, Phys. Fluids 10 (11) (1998) 2695–2697.
[19] E. Serre, E. Crespo del Arco, P. Bontoux, Annular and spiral patterns in flow between rotating and stationary disks, J. Fluid Mech. 434 (2001) 65–100.
[20] E. Serre, S. Hugues, E. Crespo del Arco, A. Randriamampianina, P. Bontoux, Axisymmetric and three-dimensional instabilities in an Ekman boundary layer flow, J. Heat Fluid Flow 22 (2001) 82–93.
[21] N. Aubry, R. Guyonnet, R. Lima, Spatiotemporal analysis of complex signals: theory and applications, J. Statist. Phys. 64 (3/4) (1991) 683–739.
[22] J.L. Lumley, Stochastic Tools in Turbulence, Academic Press, 1970.
[23] K. Karhunen, Zur Spektraltheorie stochatischer Prozesse, Ann. Acad. Sci. Fennicae Ser. A 1 (1944) 34.
[24] M. Loève, Probability Theory, Van Nostrand, New York, 1955.
[25] G. Gauthier, P. Gondret, M. Rabaud, Motion of anisotropic particles: application to visualization of three-dimensional flows, Phys. Fluids 10 (1998) 2147–2154.
[26] N. Cousin-Rittemard, O. Daube, P. Le Quéré, Sur la nature de la première bifurcation des écoulements inter-disques, C. R. Acad. Sci. Paris, Sér. IIb 326 (1998) 359–366.
[27] L. Schouveiler, P. Le Gal, M.P. Chauve, Y. Takeda, Spiral and circular waves in the flow between a rotating and a stationary disc, Exp. Fluids 26 (1999) 179–187.
[28] N. Aubry, R. Guyonnet, R. Lima, Spatio-temporal symmetries and bifurcations via the bi-orthogonal decomposition, J. Nonlinear Sci. 2 (1992) 183–215.
[29] J.E. Los, Non-normally hyperbolic invariant curves for maps in R^3 and doubling bifurcation, Nonlinearity 2 (1989) 149–174.
[30] M.R. Bassett, J.L. Hudson, Experimental evidence of period doubling of tori during an electrochemical reaction, Physica D 35 (1989) 289–298.
[31] K.E. McKell, D. Bromhead, R. Jones, D.D.J. Hurdle, Torus doubling in convecting Moltem Gallium, Europhys. Lett. 12 (6) (1990) 513–518.
[32] A.C. Skeldon, T. Mullin, Mode interaction in a double pendulum, Phys. Lett. A 166 (1992) 224.

[33] J.M. Flesselles, V. Croquette, S. Jucquois, Period doubling of a torus in a chain of oscillators, Phys. Rev. Lett. 72 (18) (1994) 2871–2874.
[34] J.C. Shin, Experimental observation of a torus-doubling transition to chaos near the ferroelectric phase transition of a KH_2PO_4 crystal, Phys. Rev. E 60 (5) (1994) 5394–5401.
[35] J. von Stamm, U. Gerdts, T. Buzug, G. Pfister, Symmetry breaking and period doubling on a torus in the VLF regime in Taylor–Couette flow, Phys. Rev. E 54 (5) (1996) 4938–4957.
[36] G. Iooss, J.E. Los, Quasi-genericity of bifurcations to high dimensional tori for maps, Commun. Math. Phys. 119 (1988) 453–500.
[37] N. Newhouse, D. Ruelle, F. Takens, Occurence of strange axiome A attractors near quasiperiodic flow on $T\hat{m}$, Commun. Math. Phys. 64 (1978) 35–40.
[38] A. Arnéodo, P. Coullet, E.A. Spiegel, Cascade of period doublings of tori, Phys. Lett. A 94 (1983) 1–6.
[39] P. Wulf, C. Egbers, H. Rath, Routes to chaos in wide gap spherical Couette flow, Phys. Fluids 11 (6) (1999) 1359–1372.
[40] H. Rasmussen, High Reynolds number flow between two infinite rotating disks, J. Aust. Math. Soc. 12 (1971) 483–501.